Inferring the Solar Wind Velocity in the Outer Corona Based on Multiview Observations of Small-scale Transients by STEREO/COR2

Shaoyu Lyu[1,2] , Yuming Wang[1,2,3] , Xiaolei Li[1,2], Quanhao Zhang[1,2,4] , and Jiajia Liu[1,2,4]

[1] Deep Space Exploration Laboratory/School of Earth and Space Sciences, University of Science and Technology of China, Hefei 230026, People's Republic of China; ymwang@ustc.edu.cn

[2] CAS Center for Excellence in Comparative Planetology/CAS Key Laboratory of Geospace Environment/Mengcheng National Geophysical Observatory, University of Science and Technology of China, Hefei 230026, People's Republic of China

[3] Hefei National Laboratory, University of Science and Technology of China, Hefei 230088, People's Republic of China

[4] Collaborative Innovation Center of Astronautical Science and Technology, Hefei 230026, People's Republic of China

Abstract

Based on the Heliospheric Imager-1 images of the STEREO twin spacecraft, we established the CORrelation-Aided Reconstruction (CORAR) technique to locate and reconstruct the 3D structures of solar wind transients in interplanetary space. Here, we extend the CORAR method to images of COR2 on board STEREO to study the evolution of small-scale transients in the outer corona from 2010 January to May. We confirm that the transients can be located and reconstructed well by comparing the results with those of a self-similar expanding model. The speed distribution of the reconstructed transients generally shows the typical characteristics of the slow solar wind. We further study the sources of the transients on the Sun, and find that most reconstructed transients are located near the top of streamer belts or the heliospheric current sheet and can be tracked back to the boundaries of the closed-field and open-field regions along the field lines extrapolated by corona models. The formation mechanisms of these transients in the slow solar wind are also discussed.

1. Introduction

The solar corona is the outer layer of the solar atmosphere. It can extend to heights of more than 10 solar radii ($R_\odot$) above the photosphere and contains complex structures, such as coronal holes, helmet streamers, and loops, which are influenced by the magnetic field geometry. The coronal plasma has a temperature of up to several 10^6 K and is comprised of free electrons, protons, alpha particles, and other ions. Visible light from the photosphere can be scattered by coronal electrons through Thomson scattering (Howard & Tappin 2009; Howard & DeForest 2012; DeForest et al. 2013; Howard et al. 2013; Inhester 2015), which allows visible wavelength coronagraphs to be widely used to make remote observations of the outflows of solar wind in the corona. For example, the Solar and Heliospheric Observatory (SOHO; Domingo et al. 1995) is equipped with the Large Angle and Spectrometric Coronagraph (LASCO; Brueckner et al. 1995) to observe the outer corona. The SECCHI suite (Howard et al. 2008) on board the Solar Terrestrial Relations Observatory (STEREO; Kaiser et al. 2008) contains two coronagraphs (COR1 and COR2) to observe simultaneously from two vantage points. More recently, the Parker Solar Probe (PSP; Fox et al. 2016), launched in 2018, has made observations of fine structures in the solar wind at closer distances to the Sun using the Wide-field Imager for Solar PRobe (WISPR; Vourlidas et al. 2016). The Solar Orbiter (SolO; Müller et al. 2020) can provide observations from an off-equator viewpoint using both a similar imager, SoloHi (Howard et al. 2020), and coronagraph, Metis (Antonucci et al. 2020).

The solar wind generally consists of a steady background outflow with embedded transient structures, and is accelerated and heated during the propagation from the corona into interplanetary space. Two main theories have been proposed to explain the dynamics: the reconnection/loop-opening (RLO) model and the wave/turbulence-driven (WTD) model. In the RLO mechanism, the energy for acceleration and heating is generally attributed to magnetic reconnection between closed and open magnetic fields connected to the Sun (Axford & McKenzie 1992; Fisk et al. 1999; Fisk 2003; Schwadron & McComas 2008; Cranmer 2009; Fisk & Kasper 2020). On the other hand, in the WTD model, the energy is assumed to be provided by wave-like fluctuations, through processes such as wave damping and turbulence cascade (Matthaeus et al. 1999; Cranmer 2005, 2009; Suzuki & Inutsuka 2006; Cranmer et al. 2007). Tied into the two mechanisms, solar wind transients may originate near the solar surface or form en route as the solar wind propagates outward (Viall et al. 2021).

Solar wind transient structures, e.g., coronal mass ejections (CMEs), shocks, blobs, and turbulence, can be observed by coronagraphs due to the inhomogeneity in the plasma density. A CME—a typical, large-scale solar wind transient originating from the Sun—can inject a significant mass of plasma into the heliosphere. Fast CMEs may generate traveling shocks when propagating in the corona and in the solar wind (Maloney & Gallagher 2011). They are capable of triggering dramatic changes of space weather if they encounter the magnetospheric system of the Earth (Gosling et al. 1990; Wang et al. 2003, 2006; Manoharan 2006; Balan et al. 2014; Shen et al. 2017; Dang et al. 2022). Meanwhile, smaller-scale transients exist in the solar wind, such as streamer waves, streamer

detachments, in/out pairs, and streamer blobs (Sheeley et al. 1997, 2009; Wang et al. 1998; Sheeley & Wang 2007; Bemporad et al. 2008; Chen et al. 2010; Sheeley & Rouillard 2010; Sanchez-Diaz et al. 2017b; López-Portela et al. 2018; Poirier et al. 2023). Magnetic switchbacks, defined as local deflections of the magnetic field combined with velocity spikes, are observed frequently by PSP in the near-Sun solar wind (Horbury et al. 2018, 2020; Kasper et al. 2019) and may be observed in coronagraph images (Telloni et al. 2022). Studying the properties and evolution of transients widely observed in the extended corona (DeForest et al. 2018) will help us understand the physical nature and origin of the solar wind in both the solar atmosphere and interplanetary space.

Based on single-view observations, the projected velocity of transients in the plane of sky (POS) can be measured by the cross-correlation analysis of images at different moments (Lewis & Simnett 2000, 2002; Ying et al. 2019). Under the assumption that the image intensity remains constant, the optical flow method was developed to measure the motion of different CME parts in successive coronagraph images (Colaninno & Vourlidas 2006). Cho et al. (2018) derived the 2D distribution of the solar wind speed by applying Fourier filtering on LASCO-C3 images. Furthermore, many techniques aim at deriving the 3D information of transients, including their positions and velocities, from remote observations. The principle of forward modeling techniques is that the kinematic parameters of transients can be estimated by fitting empirical or theoretical models (Zhao et al. 2002; Xie et al. 2004; Xue et al. 2005; Thernisien et al. 2006, 2009; Zhao 2008; Thernisien 2011). For single-view observations, one can estimate the direction and velocity of transients by trace-fitting methods. Examples of such methods include Point-P, Fixed-φ, harmonic mean, and self-similar expansion (Sheeley et al. 1999; Howard et al. 2006; Davies et al. 2012, 2013; Moestl & Davies 2013; Wang et al. 2013; Volpes & Bothmer 2015). Liewer et al. (2020 and 2023) applied a curve-fitting technique on a sequence of WISPR images to determine the direction of coronal ejecta. By employing the polarization ratio technique on polarized brightness images (Moran & Davila 2004; Dere et al. 2005; Moran et al. 2010; DeForest et al. 2017), it is possible to identify the density-weighted center of a transient along the line of sight (LOS). Through multiviewpoint observations, techniques like tie-pointing, geometric localization, mask fitting, and local correlation tracking (Pizzo & Biesecker 2004; Inhester 2006; Mierla et al. 2008, 2009, 2010; de Koning et al. 2009; Feng et al. 2012, 2013) can triangulate and determine the locations and shapes of transients. It is challenging but significant to study how to locate, trace, and reconstruct the transients widely distributed in the near-Sun solar wind.

Based on triangulation, we developed the CORrelation-Aided Reconstruction (CORAR) technique (Li et al. 2018, 2020) to automatically locate and reconstruct solar wind transients in 3D space from Heliospheric Imager-1 images taken from the twin STEREO spacecraft. Further developments to this technique allow the measurement of the radial velocity of transients, using the maximum correlation-coefficient localization and cross-correlation tracking method (Li et al. 2021). Those papers focused on heliospheric imaging data from STEREO. Meanwhile, we are trying to extend this technique to coronagraph images. We first studied the optimal separation angle of spacecraft for various solar transients (Lyu et al. 2020, 2021), and then tested and

optimized the parameters used in our reconstruction technique for coronal small-scale transients with synthetic images (Lyu et al. 2023; hereafter, Paper I). In this paper, we applied the technique to real small-scale transients observed in COR2 images.

We will introduce the data and CORAR method in Section 2, and present the results of the reconstructed small-scale transients in Section 3. In Section 4, we discuss the sources and characteristics of the reconstructed small-scale transients and their relationship with the formation of the slow solar wind (SSW). Finally, a conclusion is summarized in Section 5.

2. Method and Data

2.1. Observations by STEREO/COR2

This study is based on visible light images from the coronagraph COR2 on board STEREO. COR2 can observe the outer corona in the range of 2.5–15 $R_\odot$ in the POS. The STEREO twin spacecraft (Ahead and Behind, named STA and STB, respectively) orbit the Sun at approximately 1 au in the ecliptic plane. During 2010 Jan 1–2010 May 20 (covering the Carrington Rotation (CR) periods CR2092–CR2096), the separation angle between the STA and STB spacecraft is about 135°–150°, which favors reconstruction by the CORAR technique (Paper I). The COR2 images are processed by removing the monthly minimum background containing the F corona, denoising to reduce star and stray light, normalizing the brightness using the normalizing radial graded filter (Morgan et al. 2006), and extracting transients from quiescent coronal structures by Gauss filtering. Large-scale transients such as large CMEs are excluded from our study by manual checking. To investigate transients oriented toward the Earth, we utilize the following spatial grid: longitude/latitude spanning from −60° to 60° in the Heliocentric Earth Ecliptic (HEE) coordinates, with a resolution of 1°; and heliocentric distance ranging from $4R_\odot$ to $15R_\odot$, with a resolution of $0.02R_\odot$. Figures 1(a)–(b) presents the STA-/STB-carried COR2 (COR2A/B) images processed for reconstruction.

2.2. Principles of CORAR Technique

The CORAR technique (Li et al. 2018, 2020) requires the simultaneous and continuous observation of solar wind transients from two different viewpoints. It contains the following steps. (1) Select a meridian plane in the HEE coordinates; the observation images from two spacecraft are projected onto this plane along the LOS. The image data from COR2A and COR2B are resampled in the projected plane. (2) Compute the Pearson correlation coefficient (cc) between the two projected images, utilizing a suitably sized sampling box running through the entire plane. The distribution of cc in the plane is therefore obtained, and high cc values are indicative of transients. (3) Select other meridian planes at all possible longitudes and repeat the process above to establish the 3D distribution of cc. Regions with cc > 0.5 in the 3D space are identified as structures of solar wind transients reconstructed by the CORAR technique. The size of the sampling box in step 2 varies automatically to match the scale of the transients on the images (refer to Appendix A in Paper I). The transients on the images are distinguished based on the image intensity and reconstructed by following the above steps. To reduce unphysical structures reconstructed by the CORAR technique, only the high-cc regions, where the cc is largest among the LOSs of COR2A or COR2B, are recognized as valid structures
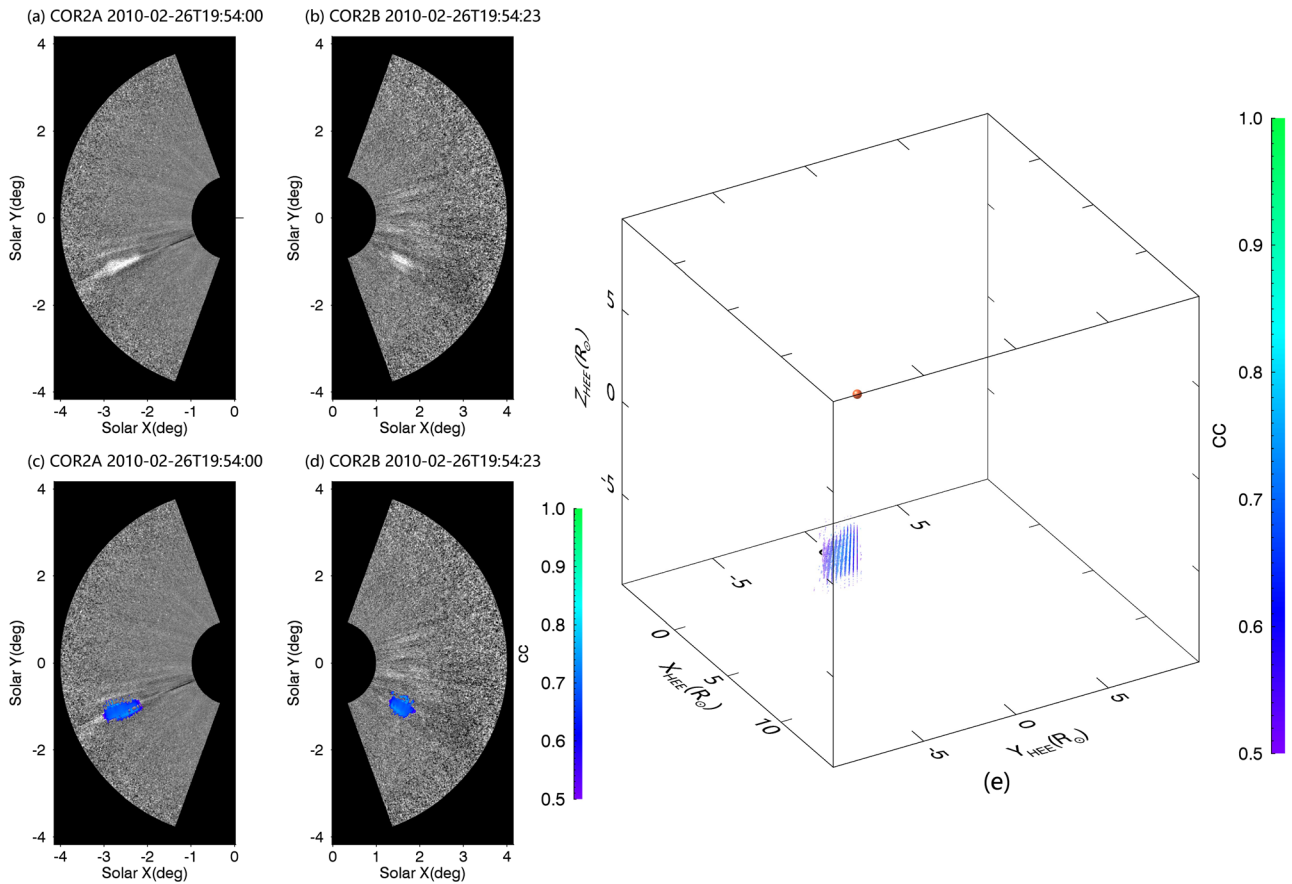
Figure 1. (a)–(b) The processed COR2 images on 2010/02/26T19:54 for the CORAR technique. (c)–(d) The same as (a)–(b), with the 2D projection of the 3D reconstructed transient. (e) The 3D structure of the reconstructed transient. For the meaning of "cc," see Section 2.2.

of transients (Li et al. 2021). Figures 1(c)–(e) present a reconstructed transient on 2010/02/26T19:54 projected on COR2 images and its structure in the 3D space.

Since our technique relies on dual-point observations, when the LOSs from two spacecraft are not (anti)parallel, the possible ambiguity of transients along the LOS from one spacecraft will be eliminated by the observation from another point of view. The scale of a reconstructed transient may be influenced by its position relative to the two spacecraft. We have investigated its impact on the reconstruction quality of small-scale transients in synthetic images in our previous study (Paper I). We found that the proportion of the number of transients with good reconstruction quality with respect to the number of all transients in a meridian plane decreases as it deviates from the central meridian plane between two space-craft. This means that transients are more likely to exhibit poor localization and reconstruction when located away from the central meridian plane. This is probably due to the central meridian plane being close to the Thomson sphere (Vourlidas & Howard 2006; Howard & DeForest 2012) of two coronagraphs when the separation angle between the spacecraft is larger than 90°.

It is noted that streamer blobs, a major type of small-scale transient, are often released periodically from the top of coronal streamers, likely through the intermittent reconnection of the coronal magnetic field, and are regarded as important sources of the SSW (Sheeley & Rouillard 2010; Rouillard et al. 2011; Viall & Vourlidas 2015; Sanchez-Diaz et al. 2017a, 2017b).

They are expected to have a flux-rope structure extending along the streamer belt, which causes it to look like a bubble along the streamer belt, but like an extended arch from the side (e.g., Sheeley & Rouillard 2010; Rouillard et al. 2011). Thus, streamer blobs can be faint or invisible on images when the streamer belt is highly inclined with respect to the observer (Poirier et al. 2023). In this work, most recognized small-scale structures look like a bubble, suggesting that the inclination of a streamer blob may affect the quality of the reconstruction of CORAR.

2.3. Radial Velocity of Transients

The velocity of transients in the 3D space is calculated by tracking their motion in consecutive images. First, for each reconstructed transient at a moment, the corresponding 2D features on the COR2A and COR2B images are recognized. Next, the central positions of the transient in the images of four other time steps (the two previous ones and the two next ones) are determined by searching the place associated with the highest cross-correlation coefficients. The 3D positions of the transient at the four other time steps are then obtained through triangulation from two viewpoints. Finally, the propagating radial velocity of the transient is obtained by fitting its heights with a linear function (with the aid of a least-squares method). For instance, Figure 2 shows the trace and fitting velocity of the reconstructed transient located at 33° in longitude, −16° in latitude, and 10.6 $R_\odot$ in heliocentric distance on 2010/02/26T19:54. Reconstructed
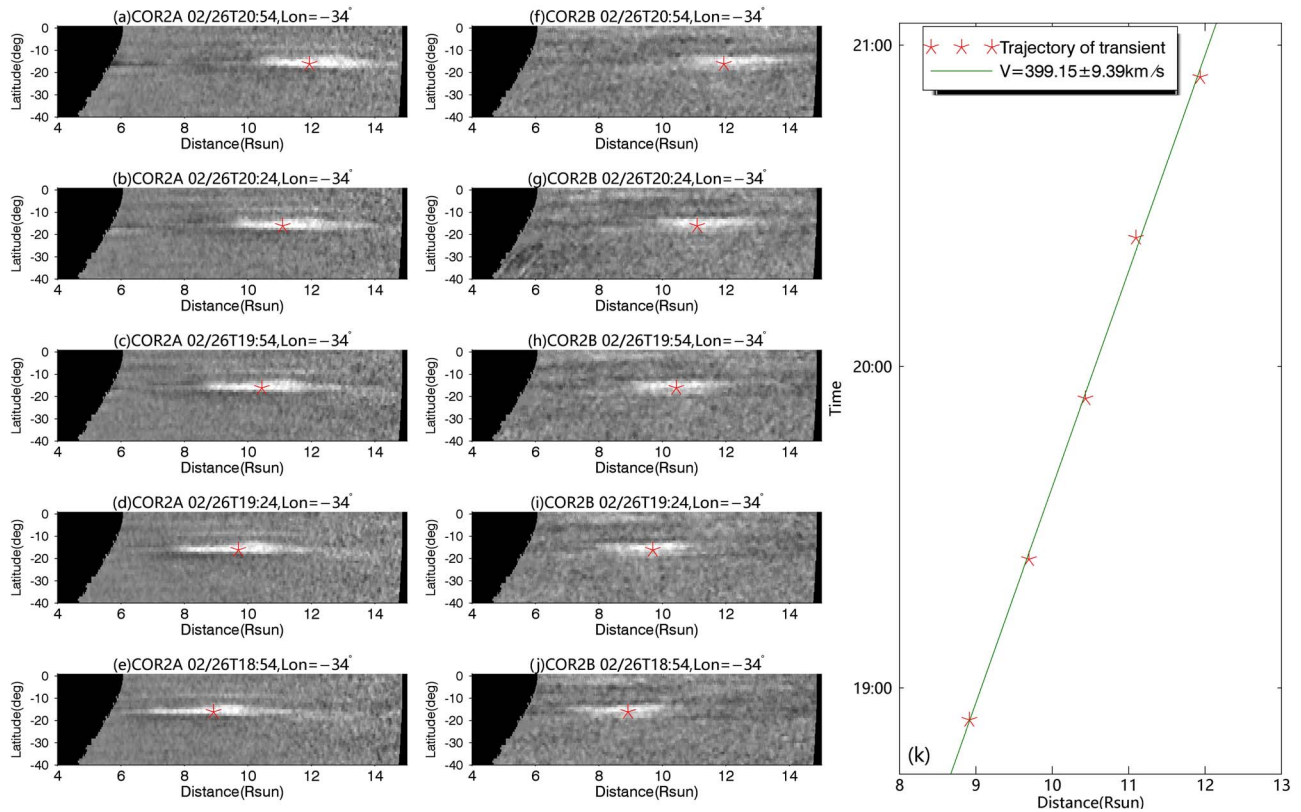
Figure 2. (a)–(e) The trace of a transient observed by COR2A. The images are projected onto the meridian plane of $33°$ in HEE longitude. The central positions of the transient calculated at different moments are marked by the red asterisks. (f)–(j) The trace of the transient observed by COR2B. (k) The central position of the transient in heliocentric distance (red asterisks) and the fitting curve for the measurement of velocity (green line).

structures at different moments are recognized as the same transient if their trajectories overlap.

The measurement error in the radial velocity could be attributed to the accuracy in locating the positions of the transients, the limitations from the grid size, and the different-apparent-leading-edge (DALE) effect from triangulation (Liewer et al. 2011). We test the accuracy in the measurement of the velocity based on synthetic observations, and find that the error varies with the longitude of the meridian plane due to the DALE effect and the inaccuracy of the location (see the Appendix).

2.4. Assessment for Recognized Transients

Our study aims at small-scale transients observed by coronagraphs, such as blobs and other density-inhomogeneous structures. It has been reported that the size of blobs is about $1R_\odot$ in the radial direction and $0.1R_\odot$ in the transverse direction at their initial stages (Sheeley et al. 1997), and magnetohydro-dynamic (MHD) simulations have suggested that blobs released from the streamer cusp have a typical scale of $0.5–2R_\odot$ in length (Endeve et al. 2003, 2004; Chen et al. 2009; Lynch 2020; Reville et al. 2020, 2022). López-Portela et al. (2018) studied 44 blobs with radial sizes ranging between $0.57R_\odot$ and $1.69R_\odot$ during propagation, while Sanchez-Diaz et al. (2017a) found a typical size of $12R_\odot \times 5R_\odot$ for the transient structure released in the SSW in the heliosphere. Here, we perform an independent evaluation of the sizes of the small-scale transients in this study. We select 51 transients that have clear features in consecutive COR2A and COR2B images simultaneously, and use a self-similar ellipsoid (SSE)

geometrical model to fit these transients to obtain their locations and shapes at different moments. The ellipsoid is assumed to keep a constant aspect ratio during the propagation. Self-similarly expanding models based on the basic principle of triangulation are widely used to derive the positions and scales of transients (Davies et al. 2013; Moestl & Davies 2013; Mishra et al. 2015; Volpes & Bothmer 2015; Barnes et al. 2020), and their results are tested to be reliable. Thus, our reconstruction results will be compared with the SSE model results in the next section to see how consistent the parameters from the two methods are. Figure 3 shows that most transients have a radial size of about $1–5R_\odot$ and a latitudinal size of about $5°–15°$ in the COR2 field of view. Therefore, we employ the following rigorous criteria to automatically identify valid transients:

1. *Morphology*. Besides real transients, there may exist unphysical structures or residual parts of real transients from reconstruction. Considering these invalid structures and the size range of the transients analyzed above, we pick up the small-scale reconstructed transients with a radial scale between $0.5R_\odot$ and $5R_\odot$, as well as a scale in longitude and latitude between $4°$ and $20°$.
2. *Continuity*. The transient must appear in five consecutive frames, and the relative 1σ error of the fitting velocity must be less than 10%.

While some valid structures may also be removed from the final data set, based on the above strict criteria, this procedure is useful for keeping the amount of unreal and incomplete transients as small as possible.
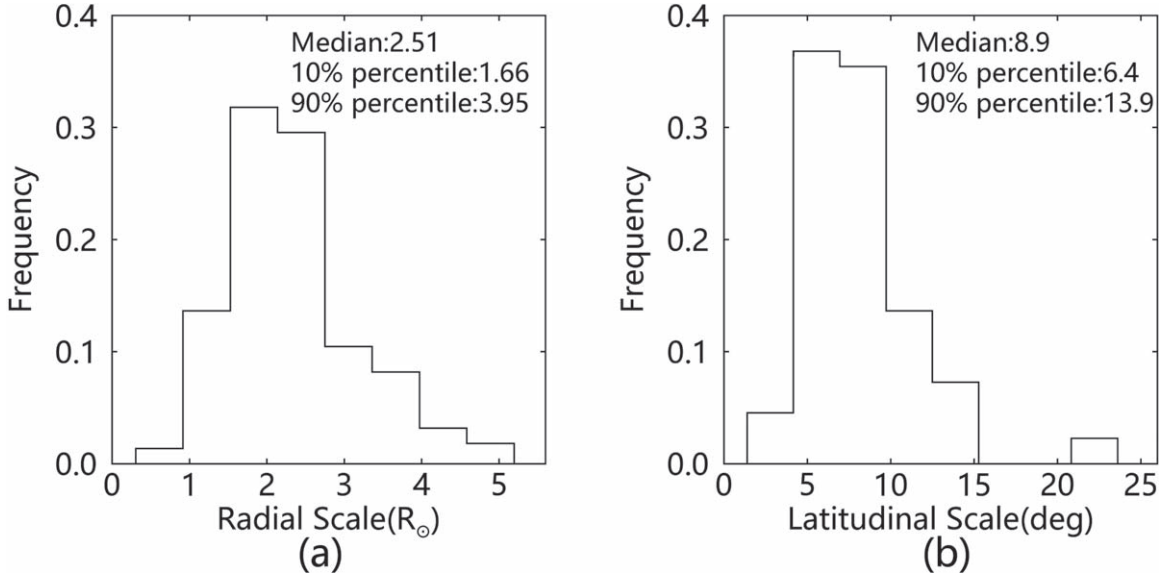
Figure 3. (a) Histogram of the values of the radial scale of the SSE model fitted for the 51 selected transients appearing in 221 frames. (b) Histogram of the values of the latitudinal scale of the SSE model. The median value and 10%/90% percentiles are shown in the images.
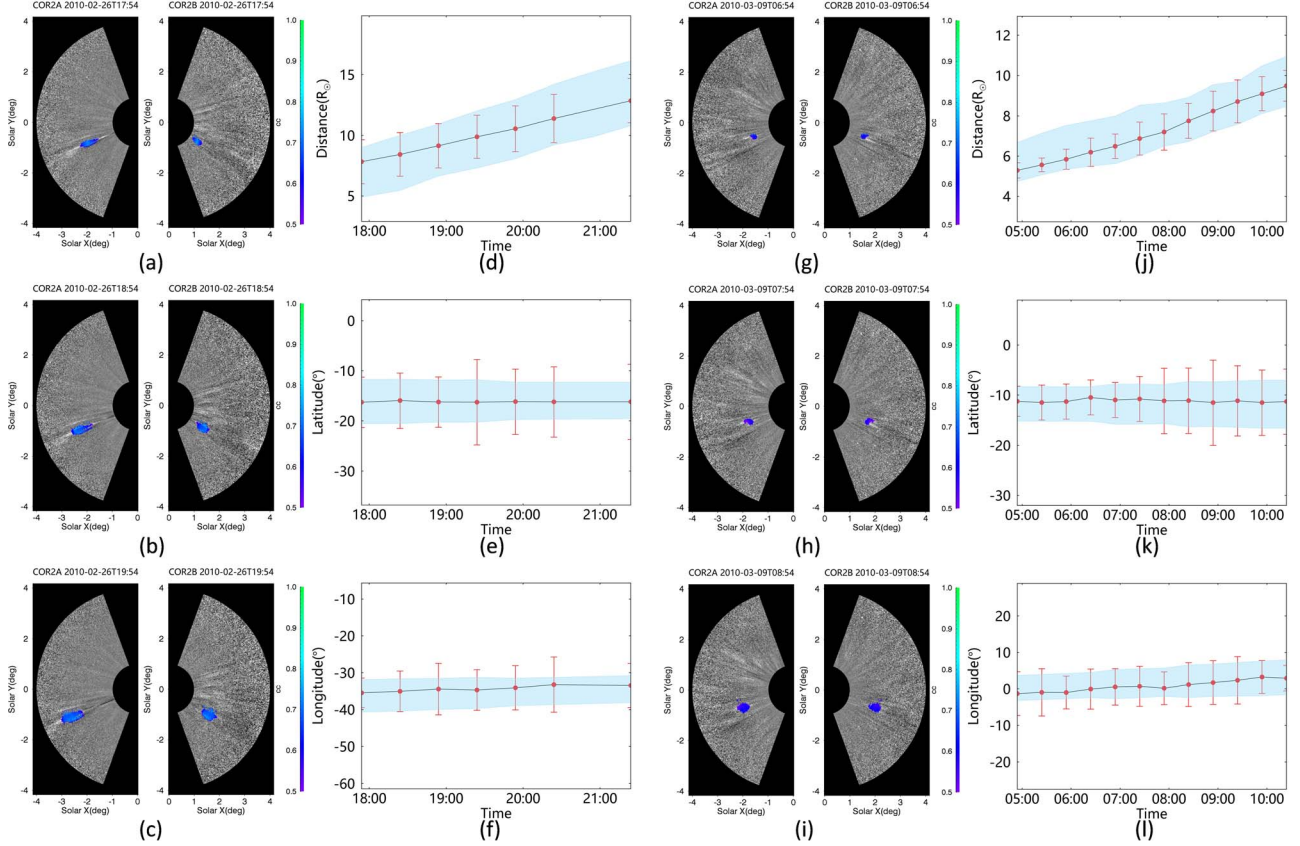

Figure 4. Examples of two reconstructed transients on 2010 February 26 ((a)–(f)) and 2010 March 9 ((g)–(l)). The transients projected on the COR2 images ((a)–(c) and (g)-(i)) are shown, and the locations of the transients in radial distance ((d) and (j)), in latitude ((e) and (k)), and in longitude ((f) and (l)) are displayed by the red points, with error bars representing the width of the reconstructed transients. The blue regions present the position and scale of the SSE models.

3. Results

3.1. Reliability of the Inferred Location and Velocity of Transients

Figure 4 displays the propagation of the location and scale of two reconstructed transients. One of them appeared in seven frames on 2010 February 26, following a slow CME on 2010 February 24. According to its position, it may be a blob generated from the cusp of a helmet streamer. The other one appeared in 12 frames on 2010 March 9. It seems to be a streamer blob or a streamer disconnection event, with a fork-like feature indicating its flux-rope geometry. To test the reliability of these reconstructed transients, we compare their shapes and positions with the results achieved by fitting the
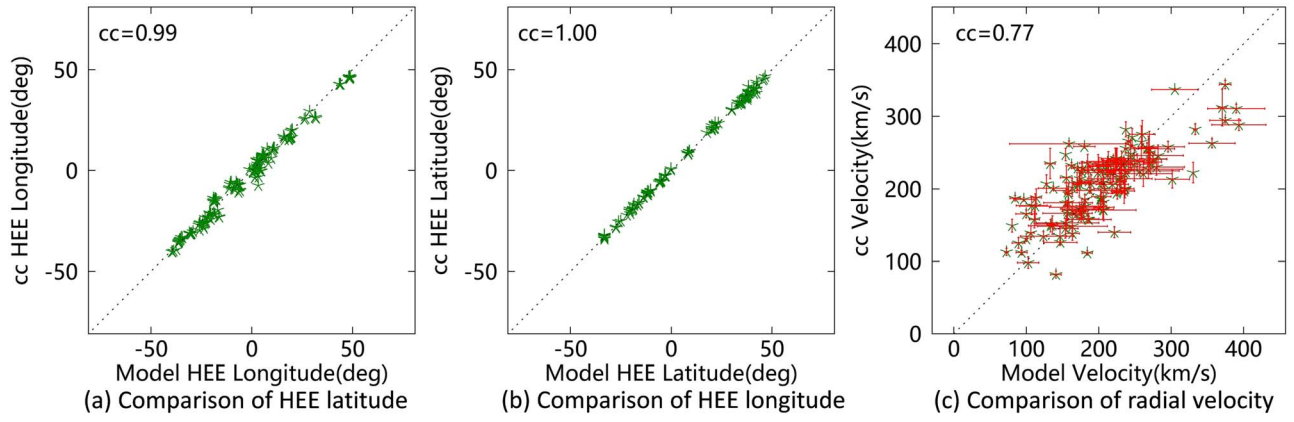
Figure 5. The comparison between the latitude (a), longitude (b), and propagating speed (c) of reconstructed transients in different frames and that of the SSE model. The dotted diagonal lines and the ccs of two results are given in the panels.
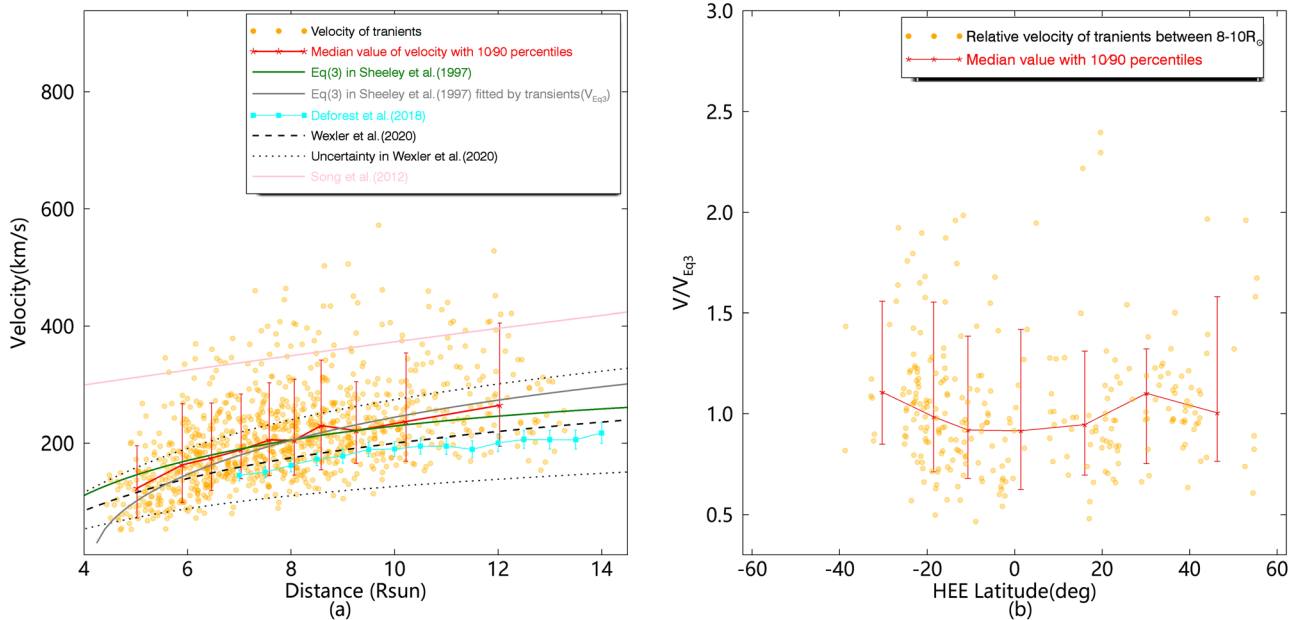

Figure 6. (a): Velocity–distance profiles (in units of $R_\odot$) for the reconstructed structures of transients at different moments (orange points). The red line with error bars represents the median value and 10%/90% percentiles of the velocity of the transients at different heights. The green line is the velocity–distance profile calculated from Equation (3) in Sheeley et al. (1997), fitted by the speed of 65 individual moving transients. The gray line shows the curve from Equation (3) in Sheeley et al. (1997), fitted by the velocity of our reconstructed transients (V_{Eq3}). The light blue line shows the trace of the transient studied in DeForest et al. (2018). The black dotted and dashed lines show the estimation of the solar wind velocity and its uncertainty boundaries through transcorona radio emission in Wexler et al. (2020). The pink line shows the empirical curve in Song et al. (2012), distinguishing post-CME blobs from streamer blobs. (b) The normalized velocity of the reconstructed transients at 8–10 $R_\odot$ by the velocity–distance profile of V_{Eq3} shown in (a) as a function of latitude. The median values and 10%/90% percentiles for the scattered points in different latitude intervals are shown in the panel.

SSE model. The locations from our method (the red points with error bars) are well consistent with those based on the SSE model (the blue area). The uncertainties of our reconstruction technique are larger than the SSE model results, except for the scale of structures in the radial direction.

Furthermore, we test the reliability of the inferred location and the velocity of the reconstructed structures of the transients selected in Section 2.4. Figure 5 presents the comparison of the latitude, longitude, and radial velocity of our results with the SSE model results. The values of cc for latitude and longitude are close to 1, and that for velocity is about 0.77, which is still high. The results mean that our reconstruction technique works well. In other words, small-scale transients in the outer corona can be detected, located, and tracked well by the CORAR technique, and the derived velocity is reasonable.

3.2. Radial Velocity Distribution of Transients

Based on the procedure described in Section 2.4, we finally recognize 624 small-scale transients in 950 frames. For these transients recognized by our technique, we can get their velocity distribution along the distance ranging from $4R_\odot$ to $14R_\odot$, as indicated by the orange dots in Figure 6(a). Generally, the velocity of the reconstructed transients increases with the increasing distance from the Sun. By setting 10 bins with an equal number of data points, we also show the median value and 10%/90% percentiles of the velocities with the red line and error bars in this figure. It is found that the red profile generally matches with the previously studied velocity distribution of small-scale transients observed by coronagraphs (Sheeley et al. 1997; DeForest et al. 2018) and that of the SSW calculated through the transcoronal radio emission (Wexler et al. 2020).

The differences are that our velocity is smaller than the velocity profiles from Sheeley et al. (1997) below 7 $R_\odot$, but it becomes larger when exceeding 7 $R_\odot$. Compared with the velocities from DeForest et al. (2018) and Wexler et al. (2020), our velocities are systematically larger by about 50 km s^{-1}.

The larger median value of the velocity by our method is partially due to some high-speed transients with small scales. For instance, the narrow CMEs, defined arbitrarily as events whose apparent angular width is smaller than 20°, may have large speeds similar to the normal CMEs (Gilbert et al. 2001; Mittal et al. 2009). Those small CMEs are probably recognized as small-scale transients and are hardly manually excluded from our sample. Meanwhile, Song et al. (2012) pointed out that streamer blobs and post-CME blobs exhibit differences in formation and propagation. Streamer blobs are generally found at the tips of coronal streamers and exhibit velocities similar to the background solar wind. On the other hand, post-CME blobs are generated from the accompanying current sheet formed after the CME eruption, and their velocity is generally larger and scatters more than that of the streamer blobs. Based on an empirical function that distinguishes these two types of blobs, proposed in Song et al. (2012), about 94% of the reconstructed structures in our study belong to the relatively low-speed streamer blob type. Therefore, most reconstructed transients can be considered as tracers of the background slow wind.

Another possible reason for the large velocity of some transients is the influence of the fast solar wind (FSW) from mid- or high-latitude regions. To analyze the velocity distribution of transients at different latitudes, we normalize the velocity of the reconstructed transients at different heights by the velocity–distance profile presented in Sheeley et al. (1997):

$$V^2 = V_a^2 (1 - e^{-\frac{r-r_1}{r_a}}). \quad (1)$$

Sheeley et al. (1997) got $V_a = 298.3$ km s^{-1}, $r_1 = 2.8 R_\odot$, and $r_a = 8.1 R_\odot$ by fitting the speed of 65 individual moving transients (the green line in Figure 6(a)), and we get $V_a = 408.9$ km s^{-1}, $r_1 = 4.2 R_\odot$, and $r_a = 13.2 R_\odot$ by fitting the velocity of the reconstructed transients (the gray line in Figure 6(a), named as V_{Eq3}). Comparing the velocity of the transients normalized by V_{Eq3}, we find that transients at higher latitude tend to be faster than those at lower latitude (Figure 6(b)). This could be attributed to the fact that some transients are generated near the high-latitude FSW. In summary, the evolution of the reconstructed transients partially reflects the propagation characteristics of the solar wind.

4. Discussion

The solar wind can be divided into two main categories: the FSW and the SSW. Compared with the FSW generally originating from coronal holes, the SSW tends to be highly variable in plasma density, velocity, and composition (Abbo et al. 2016). It is important to investigate where the reconstructed transients originate from and how the sources of solar wind influence the properties of these transients.

4.1. Source Regions of Transients Tracked through Field Extrapolation

Figures 7(a)–(e) display the location of 595 reconstructed transients during the CR periods from 2092 to 2096 (2010

January 3–2010 May 19), compared with synoptic maps of the white-light corona at the height of $5R_\odot$. The synoptic maps are generated by COR2A observations. During this time interval in the increasing phase of Solar Cycle 24, the sunspot number does not increase monotonically, while the number of reconstructed transients increases with the CR number, except for CR2094 (Table 1). Besides the influence from the increasing phase of solar activities, the change of the inclination of streamer belts may be another reason (see Section 2.2). It was observed that a majority of the small-scale transients originate from the coronal streamer belt (the long strips in the longitude direction shown in Figures 7(a)–(e)), indicating that these transients are primarily associated with the solar wind originating from low-latitude coronal streams, in line with the characteristics of the SSW. We also study the relationship between reconstructed transients and the coronal magnetic field (Figures 7(f)–(j)). The magnetic field in the corona below the source surface ($r_s = 2.5R_\odot$) is extrapolated by the PFSS model, and the field in the extended corona ($2.5R_\odot < r < 21.5R_\odot$) is generated by the Schatten current sheet (SCS) model (Schatten 1971). The inner boundary conditions at the solar surface are the magnetograms from the Global Oscillations Network Group (GONG). They are generated as parts of the Wang–Sheeley–Arge (WSA) model (Arge & Pizzo 2000) in the Community Coordinated Modeling Center. It is found that about 80% of transients are located within 20° from the heliospheric current sheet (HCS), and more than 98% of transients are traced back to footpoints within 5° of the nearest boundaries between the open- and closed-field regions on the photosphere.

The sources of most reconstructed transients suggest that they are possibly generated by magnetic reconnection. One theory for the formation of the SSW is that the closed-field plasma is released into the SSW by the interchange reconnection between the open field in the coronal hole with nearby closed coronal loops (Fisk 2003; Edmondson 2012; Fisk & Kasper 2020; Raouafi et al. 2023). In this mechanism, the momentum and energy for the SSW is provided by the magnetic reconnection and the Lorentz force in the low corona. Higginson & Lynch (2018) presented an MHD simulation showing that the interchange reconstruction scenario can generate "pseudo-flux-rope" structures in the SSW. Griton et al. (2020) suggested that the interchange reconnection related to the coronal bright points is a good candidate for explaining the small density fluctuations on a timescale of less than 60 minutes (DeForest et al. 2018). Furthermore, the S-web model proposed by Antiochos et al. (2011) proposed that the source of the SSW is a network of narrow open-field corridors that map to a web of separatrix surfaces and quasi-separatrix layers in the heliosphere. In the topology of the S-web, the boundary layers between the open and closed magnetic flux have large arcs extending along the longitude (Higginson et al. 2017; Scott et al. 2018). The SSW is released from the arcs through interchange reconnection (Baker et al. 2023; Chitta et al. 2023), or possibly related to the high expansion rate discussed in Section 4.2.

Meanwhile, mechanisms like pinch-off reconnection, diffusion, or thermal instabilities can release the plasma restrained by the closed field into the solar wind, leading to the generation of streamer blobs (Wang et al. 1998; Sheeley et al. 2009; Sheeley & Rouillard 2010; Sanchez-Diaz et al. 2017a, 2017b; López-Portela et al. 2018; Nindos et al. 2021). In this case, the
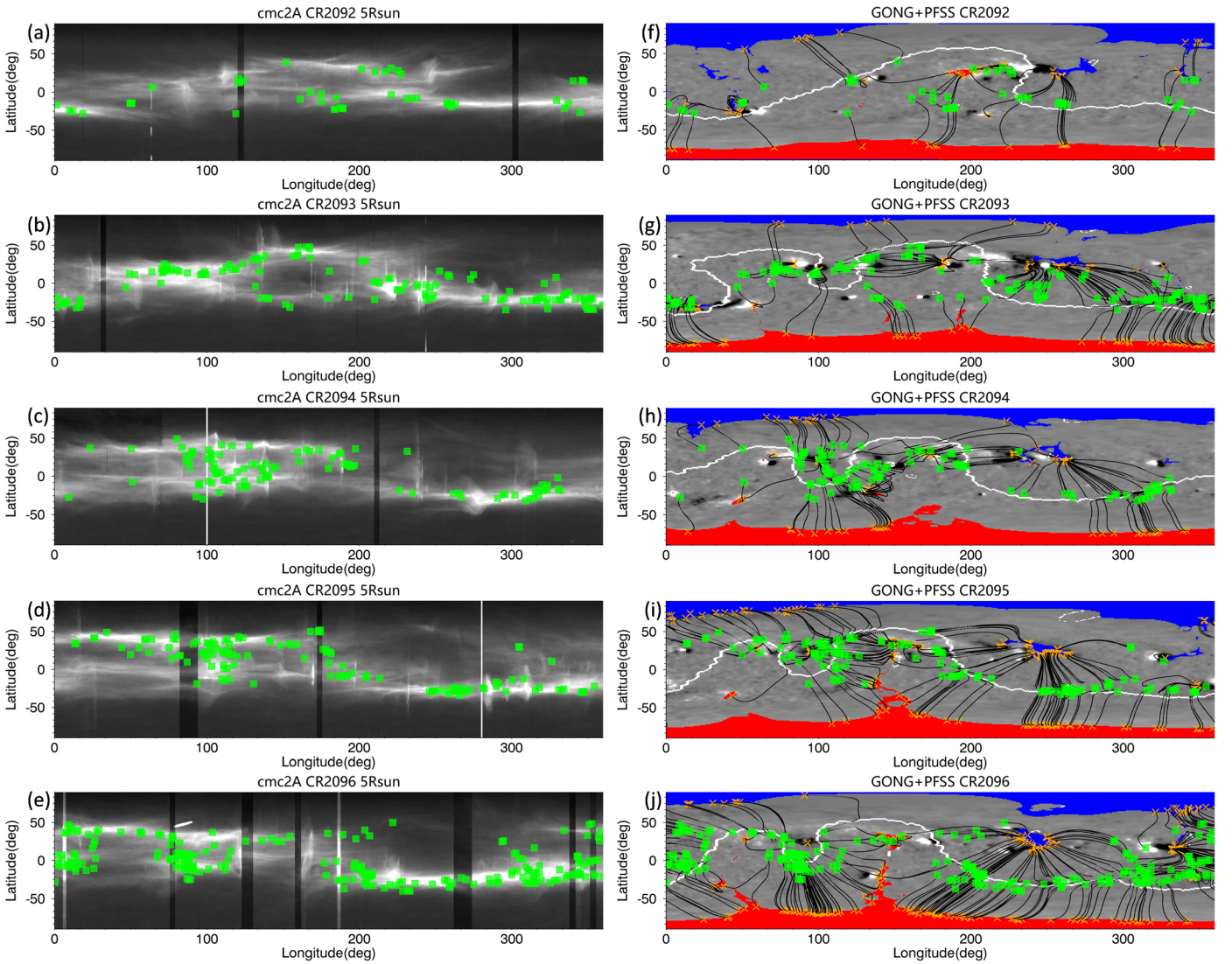
Figure 7. (a)–(e) Synoptic maps of the corona at $5R_{\odot}$, with the positions of the transients (green squares) projected on the full map in different CR periods. The maps are generated from the COR2A images. (f)–(j) The tracing field lines of the reconstructed transients. The transients are marked by the green squares, and their estimated source regions on the solar surface are marked by the orange forks. The magnetic field is extrapolated by the PFSS and SCS models from the GONG magnetograms displayed as background maps. The positive/negative open-field regions are marked in red/blue color. The white lines are polarity inversion lines derived from the extrapolated magnetic field at $2.5R_{\odot}$.

Table 1
Number of Transients and Sunspots during Different CR Periods

CR Number	Sunspot Number	Number of Transients
2092	548	51
2093	786	124
2094	591	100
2095	456	129
2096	258	191

Note. Sunspot data are from the World Data Center SILSO, Royal Observatory of Belgium, Brussels.

reconnection occurs at the cusp of helmet streamers, which is different from the interchange reconnection in the lower solar atmosphere. One form of observational evidence for this process is the quasiperiodic behavior reported in many studies. Viall & Vourlidas (2015) reported a periodicity of about 65–100 minutes for the periodic density structures occurring near streamers. Kepko et al. (2016) studied the

90 minute periodic structures detected in the slow wind at the L1 point. Sanchez-Diaz et al. (2017a) found a profusion of blobs released from the HCS with an average periodicity of 19.5 hr. The generation mechanism of blobs is supported by MHD simulations (Endeve et al. 2003, 2004; Chen et al. 2009; Allred & MacNeice 2015; Lynch 2020; Reville et al. 2020, 2022; Poirier et al. 2023). Results from the MHD models including thermal conduction suggested that the coronal heating rate controls the periodicity (Endeve et al. 2003, 2004; Allred & MacNeice 2015). Reville et al. (2020) proposed that the tearing reconnection process is able to explain the long and short timescales of the density structures observed in the SSW, and Reville et al. (2022) found from MHD simulations that the time to thin the current sheet and trigger the reconnection is related to the Lundquist number. Therefore, the periodicity of the transients is strongly related to the coronal conditions and formation mechanisms, and may be a clue to studying their origins. However, in this study, we do not have enough information about the periodicity of the
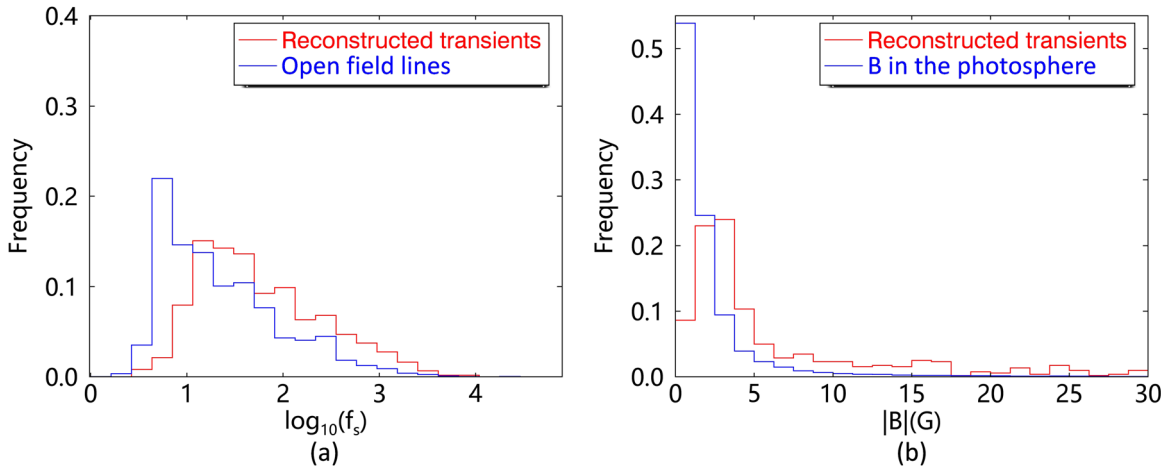
Figure 8. (a) Frequency histogram of the expansion factor f_s related to reconstructed transients (red line) and f_s of the open field lines extrapolated into the outer corona during five CR periods (blue line). The field lines are evenly sampled on the spherical surface of $21.5R_\odot$. (b) Frequency histogram of the magnetic strength of footpoints. The blue line is the histogram of $|B|$ evenly sampled in the photosphere.

investigated small-scale transients, leaving their origins ambiguous.

4.2. Properties of Magnetic Field Connecting to the Transients

Based on the synoptic map of the expansion factor (f_s) calculated from the extrapolated magnetic field, we compare the histogram of the transient-related f_s with the histogram of f_s for the open field lines evenly distributed on the spherical surface of $21.5R_\odot$ (Figure 8(a)). f_s is defined as the expansion rate of a flux tube in a solid angle between the photosphere and the source surface. We find that the f_s value of more than 92% of these slow-wind transients is larger than 10, and the mean f_s of the transients is larger than that of all field lines in the outer corona. This feature corresponds with the comparison between the extrapolation of the coronal magnetic field and the in situ measurements of solar wind speed (Wang & Sheeley 1990). When f_s is large, the field strength falls off rapidly with height, the heating is concentrated near the coronal base, and most of the energy is deposited into the transition region, so that the energy for wind acceleration in the higher corona is reduced, leading to the SSW (Leer & Holzer 1980; Cranmer 2005; Cranmer et al. 2007). In this case, the SSW is governed by the same acceleration and heating process as the FSW, which is different from the reconnection mechanism introduced in Section 4.1. The majority of coronal flux tubes expand monotonically, while some open flux tubes in the vicinity of pseudo-streamers diverge first and reconverge above a certain height, leading to low f_s with the SSW (Riley & Luhmann 2012). This suggests that f_s should be replaced by $f_{s,max}$, defined as the maximum value of the expansion rate along the flux tube, for empirical solar wind models with pseudo-streamer boundaries (Abbo et al. 2016). Therefore, we also investigate the frequency histogram of $f_{s,max}$. It is similar to that of f_s displayed in Figure 8(a), indicating a minority of reconstructed transients in the vicinity of pseudo-streamers.

Since the magnetic energy injected into the corona is one of the drivers of the solar wind, it is important to study other magnetic properties of the sources of transients. The study by Pinto et al. (2016) has confirmed that the asymptotic speed of the SSW is also strongly dependent on the field line inclination and magnetic field amplitude at the footpoints. Berezin & Tlatov (2022) found that a smaller magnetic field strength at the

base of the tube corresponds to faster winds. It is presented in Figure 8(b) that the base magnetic field strength related to the reconstructed transients has a different distribution from the overall magnetic field on the photosphere. A fraction of transients have a strong base magnetic field. This indicates that the magnetic flux emerging from the Sun is important for the SSW formation, and the origin of many transients is close to the active regions with a closed magnetic field, which matches their sources displayed in Figure 7.

5. Conclusions

In this paper, we have investigated the application of the CORAR technique, an automated 3D triangulation method, on the small-scale transients observed by COR2 on board STEREO during 2010 January–May. We recognize 950 small-scale transients using our technique, and the obtained parameters of the recognized transients are consistent with the results of a self-similar expanding model. Based on these recognized transients, we have found that most of them distribute along the typical profile of the SSW, suggesting that the small-scale transients can be treated as tracers of the background solar wind. We also notice that a few of them have higher speeds. Those high-speed transients possibly either originate from the higher-latitude regions where the FSW is expected or are fast transients, such as narrow CMEs or post-CME blobs.

The analysis of the source regions of the transients further shows that most transients are released in the vicinity of the HCS. This suggests that these transients form either at the cusp of helmet streamers or at open/closed magnetic field boundaries through interchange reconnection occurring in the lower solar atmosphere. Meanwhile, the coronal flux-tube expansion may have an influence on the propagation of solar wind transients. Besides, the magnetic field strength at the footprints of the magnetic field lines connecting to some recognized transients is generally strong, implying that the magnetic energy initially released during the formation of transients plays a role. Once transients are released into the wind, the drag force from the background flows may be a notable driving force.

The observational data from STEREO-B have been lost since 2014, so the next step for our study is to develop the

CORAR technique for processing the coronagraph data from STEREO-A and SOHO. The CORAR technique is also suitable for future space science missions equipped with multiple coronagraphs, e.g., the Solar Ring mission, consisting of three spacecraft separated by 120° on a 1 au orbit (Wang et al. 2023). Furthermore, we hope to obtain and study the properties of the reconstructed transients, including the velocity, density, temperature, magnetic field fluctuations, elemental abundance, ion charge states, and so on, by linking transients observed in coronagraphs with the in situ measurement of the near-Sun solar wind provided by PSP (Fox et al. 2016) and SolO (Müller et al. 2020).

Appendix

To test the rationality of our velocity measurement, we utilize the CORAR technique to locate and reconstruct synthetic transients defined by a sphere model (Li et al. 2020; Paper I). The separation between the two STEREO spacecraft is 135°. The transients have a radius of $0.6R_\odot$ and are located at $10R_\odot$ from the Sun, separated by 20° in latitude and longitude. The velocity is defined as 250 km s^{-1} and the central density is 5×10^4 cm^{-3}. Figure A1(a) shows the absolute error of the velocity of these transients. It suggests that the relative error in velocity is lower than 10% for all detected transients and 4% for most transients. Some transients located away from the central meridian plane are not detected by our technique. Meanwhile, some are located inaccurately, leading to a larger error of the measured velocity. This is due to the limitations of the COR2 field of view and the Thomson spheres of the coronagraphs. If the transients are located away from the Thomson spheres of COR2A and COR2B, they will be faint in images, and are less likely to be detected or located by the CORAR technique.

In our previous study (Li et al. 2021), we suggested that the error in the determination of the radial velocity of the transients by CORAR is also related to the limitations from the radial size of the grid cells and the DALE effect from triangulation (Liewer et al. 2011). The former is about 4km s^{-1}, related to the half radial size of the 3D grid cell ($0.01R_\odot$) and the cadence of the COR2 images used for reconstruction (30 minutes). The latter arises because different parts of the leading edge of the same transient observed from two spacecraft are mistaken as the same part of the transient. According to the analysis in the appendix of Liewer et al. (2011), the DALE error is related to the propagation longitude, size, and position of the transient and the separation angle between two spacecraft. As the propagation direction relative to the Sun–Earth line increases, the theoretical relative error calculated according to the scales and positions of the synthetic transients decreases at first and
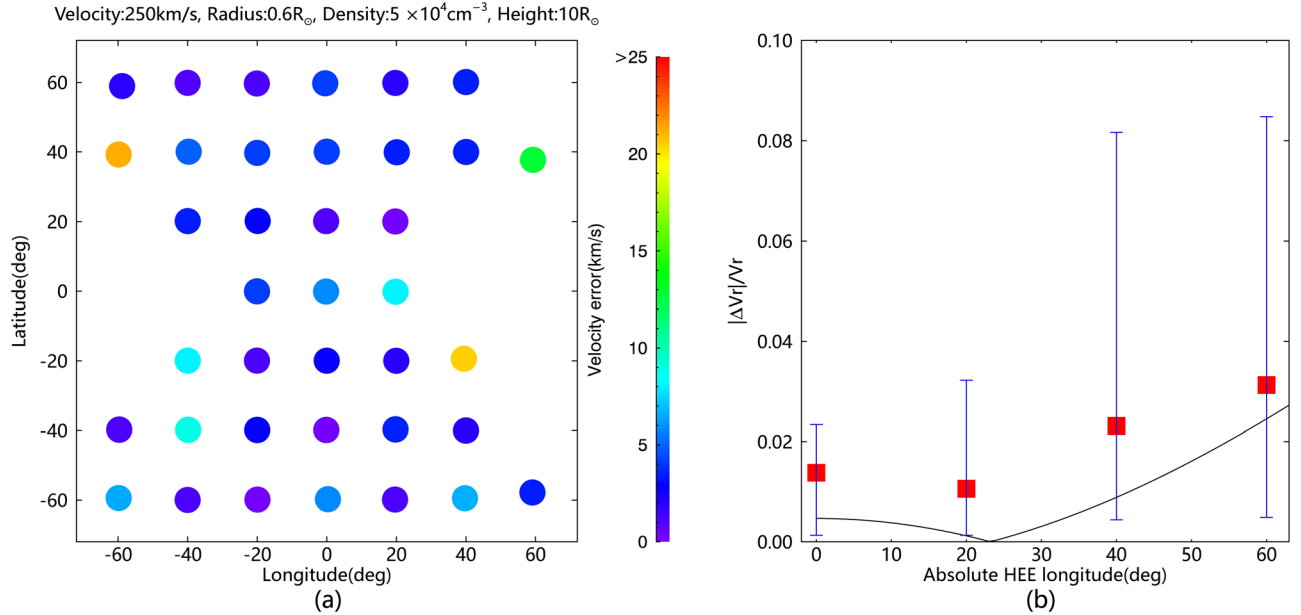

Figure A1. (a) The distribution of the absolute error in radial velocity of the synthetic transients at $10R_\odot$ from the Sun. The locations of the reconstructed transients are shown in the panel. (b) The profile of the DALE relative error (black line) as a function of the absolute longitude in HEE coordinates. It is calculated by the equation shown in Liewer et al. (2011), based on the scales and positions of the synthetic transients. The red squares with error bars present the mean, minimum, and maximum values of the relative velocity errors of the transients in the different longitude intervals shown in (a).

then increases after 23°, as shown in Figure A1(b). The statistical error of the reconstructed transients has a similar trend as the theoretical profile, and their difference is possibly related to the inaccuracy of the locations and the measuring error from the grid size.

ORCID iDs

Shaoyu Lyu ⓘ https://orcid.org/0000-0002-2349-7940
Yuming Wang ⓘ https://orcid.org/0000-0002-8887-3919
Quanhao Zhang ⓘ https://orcid.org/0000-0003-0565-3206
Jiajia Liu ⓘ https://orcid.org/0000-0003-2569-1840

References

Abbo, L., Ofman, L., Antiochos, S.K., et al. 2016, SSRv, 201, 55
Allred, J. C., & MacNeice, P. J. 2015, CS&D, 8, 015002
Antiochos, S. K., Mikić, Z., Titov, V. S., Lionello, R., & Linker, J. A. 2011, ApJ, 731, 112
Antonucci, E., Romoli, M., Andretta, V., et al. 2020, A&A, 642, A10
Arge, C. N., & Pizzo, V. J. 2000, JGRA, 105, 10465
Axford, W. I., & McKenzie, J. F. 1992, in Solar Wind Seven, ed. E. Marsch & R. Schwenn (Amsterdam: Pergamon)
Baker, D., Démoulin, P., Yardley, S. L., et al. 2023, ApJ, 950, 65
Balan, N., Skoug, R., Tulasi Ram, S., et al. 2014, JGRA, 119, 10041
Barnes, D., Davies, J. A., Harrison, R. A., et al. 2020, SoPh, 295, 150
Bemporad, A., Poletto, G., Landini, F., & Romoli, M. 2008, AnGeo, 26, 3017
Berezin, I., & Tlatov, A. 2022, Univ, 8, 646
Brueckner, G. E., Howard, R. A., Koomen, M. J., et al. 1995, SoPh, 162, 357
Chen, Y., Li, X., Song, H. Q., et al. 2009, ApJ, 691, 1936
Chen, Y., Song, H. Q., Li, B., et al. 2010, ApJ, 714, 644
Chitta, L. P., Seaton, D. B., Downs, C., DeForest, C. E., & Higginson, A. K. 2023, NatAs, 7, 133
Cho, I.-H., Moon, Y.-J., Nakariakov, V. M., et al. 2018, PhRvL, 121, 075101
Colaninno, R. C., & Vourlidas, A. 2006, ApJ, 652, 1747
Cranmer, S. R. 2005, in Solar Wind 11/SOHO 16, Connecting Sun and Heliosphere, 592 ed. B. Fleck, T. H. Zurbuchen, & H. Lacoste (Paris: ESA), 159
Cranmer, S. R. 2009, LRSP, 6, 3
Cranmer, S. R., van Ballegooijen, A. A., & Edgar, R. J. 2007, ApJS, 171, 520
Dang, T., Li, X., Luo, B., et al. 2022, SpWea, 20, e2022SW003152
Davies, J. A., Harrison, R. A., Perry, C. H., et al. 2012, ApJ, 750, 23
Davies, J. A., Perry, C. H., Trines, R. M. G. M., et al. 2013, ApJ, 777, 167
DeForest, C. E., de Koning, C. A., & Elliott, H. A. 2017, ApJ, 850, 130
DeForest, C. E., Howard, R. A., Velli, M., Viall, N., & Vourlidas, A. 2018, ApJ, 862, 18
DeForest, C. E., Howard, T. A., & Tappin, S. J. 2013, ApJ, 765, 44
de Koning, C. A., Pizzo, V. J., & Biesecker, D. A. 2009, SoPh, 256, 167
Dere, K. P., Wang, D., & Howard, R. 2005, ApJL, 620, L119
Domingo, V., Fleck, B., & Poland, A. I. 1995, SSRv, 72, 81
Edmondson, J. K. 2012, SSRv, 172, 209
Endeve, E., Holzer, T. E., & Leer, E. 2004, ApJ, 603, 307
Endeve, E., Leer, E., & Holzer, T. E. 2003, ApJ, 589, 1040
Feng, L., Inhester, B., & Mierla, M. 2013, SoPh, 282, 221
Feng, L., Inhester, B., Wei, Y., et al. 2012, ApJ, 751, 18
Fisk, L. A. 2003, JGRA, 108, 1157
Fisk, L. A., & Kasper, J. C. 2020, ApJL, 894, L4
Fisk, L. A., Schwadron, N. A., & Zurbuchen, T. H. 1999, JGRA, 104, 19765
Fox, N. J., Velli, M. C., Bale, S. D., et al. 2016, SSRv, 204, 7
Gilbert, H. R., Serex, E. C., Holzer, T. E., MacQueen, R. M., & McIntosh, P. S. 2001, ApJ, 550, 1093
Gosling, J. T., Bame, S. J., Mccomas, D. J., & Phillips, J. L. 1990, GeoRL, 17, 901
Griton, L., Pinto, R. F., Poirier, N., et al. 2020, ApJ, 893, 64
Higginson, A. K., Antiochos, S. K., DeVore, C. R., Wyper, P. F., & Zurbuchen, T. H. 2017, ApJL, 840, L10
Higginson, A. K., & Lynch, B. J. 2018, ApJ, 859, 6
Horbury, T. S., Matteini, L., & Stansby, D. 2018, MNRAS, 478, 1980
Horbury, T. S., Woolley, T., Laker, R., et al. 2020, ApJS, 246, 45
Howard, R. A., Moses, J. D., Vourlidas, A., et al. 2008, SSRv, 136, 67
Howard, R. A., Vourlidas, A., Colaninno, R. C., et al. 2020, A&A, 642, A13
Howard, T. A., & DeForest, C. E. 2012, ApJ, 752, 130
Howard, T. A., & Tappin, S. J. 2009, SSRv, 147, 31
Howard, T. A., Tappin, S. J., Odstrcil, D., & DeForest, C. E. 2013, ApJ, 765, 45
Howard, T. A., Webb, D. F., Tappin, S. J., Mizuno, D. R., & Johnston, J. C. 2006, JGRA, 111, A04105
Inhester, B. 2006, arXiv:astro-ph/0612649
Inhester, B. 2015, arXiv:1512.00651
Kaiser, M. L., Kucera, T. A., Davila, J. M., et al. 2008, SSRv, 136, 5
Kasper, J. C., Bale, S. D., Belcher, J. W., et al. 2019, Natur, 576, 228
Kepko, L., Viall, N. M., Antiochos, S. K., et al. 2016, GeoRL, 43, 4089
Leer, E., & Holzer, T. E. 1980, JGR, 85, 4681
Lewis, D. J., & Simnett, G. M. 2000, MNRAS, 317, 1005
Lewis, D. J., & Simnett, G. M. 2002, MNRAS, 333, 969
Li, X., Wang, Y., Guo, J., Liu, R., & Zhuang, B. 2021, A&A, 649, A58
Li, X., Wang, Y., Liu, R., et al. 2020, JGRA, 125, e2019JA027513
Li, X. L., Wang, Y., Liu, R., et al. 2018, JGRA, 123, 7257
Liewer, P. C., Hall, J. R., Howard, R. A., et al. 2011, JASTP, 73, 1173
Liewer, P. C., Qiu, J., Penteado, P., et al. 2020, SoPh, 295, 140
Liewer, P. C., Vourlidas, A., Stenborg, G., et al. 2023, ApJ, 948, 24
López-Portela, C., Panasenco, O., Blanco-Cano, X., & Stenborg, G. 2018, SoPh, 293, 99
Lynch, B. J. 2020, ApJ, 905, 139
Lyu, S., Li, X., & Wang, Y. 2020, AdSpR, 66, 2251
Lyu, S., Wang, Y., Li, X., et al. 2021, ApJ, 909, 182
Lyu, S., Wang, Y., Li, X., & Zhang, Q. 2023, A&A, 672, A100
Maloney, S. A., & Gallagher, P. T. 2011, ApJL, 736, L5
Manoharan, P. K. 2006, SoPh, 235, 345
Matthaeus, W. H., Zank, G. P., Oughton, S., Mullan, D. J., & Dmitruk, P. 1999, ApJL, 523, L93
Mierla, M., Davila, J., Thompson, W., et al. 2008, SoPh, 252, 385
Mierla, M., Inhester, B., Antunes, A., et al. 2010, AnGeo, 28, 203
Mierla, M., Inhester, B., Marqué, C., et al. 2009, SoPh, 259, 123
Mishra, W., Srivastava, N., & Singh, T. 2015, JGRA, 120, 10221
Mittal, N., Pandey, K., Narain, U., & Sharma, S. S. 2009, Ap&SS, 323, 135
Moestl, C., & Davies, J. A. 2013, SoPh, 285, 411
Moran, T. G., & Davila, J. M. 2004, Sci, 305, 66
Moran, T. G., Davila, J. M., & Thompson, W. T. 2010, ApJ, 712, 453
Morgan, H., Habbal, S. R., & Woo, R. 2006, SoPh, 236, 263
Müller, D., Cyr, O. C. St., Zouganelis, I., et al. 2020, A&A, 642, A1
Nindos, A., Patsourakos, S., Vourlidas, A., et al. 2021, A&A, 650, A30
Pinto, R. F., Brun, A. S., & Rouillard, A. P. 2016, A&A, 592, A65
Pizzo, V. J., & Biesecker, D. A. 2004, GeoRL, 31, L21802
Poirier, N., Réville, V., Rouillard, A. P., Kouloumvakos, A., & Valette, E. 2023, A&A, 677, A108
Raouafi, N. E., Stenborg, G., Seaton, D. B., et al. 2023, ApJ, 945, 28
Réville, V., Fargette, N., Rouillard, A. P., et al. 2022, A&A, 659, A110
Réville, V., Velli, M., Rouillard, A. P., et al. 2020, ApJL, 895, L20
Riley, P., & Luhmann, J. G. 2012, SoPh, 277, 355
Rouillard, A. P., Sheeley Jr., N. R., Cooper, T. J., et al. 2011, ApJ, 734, 7
Sanchez-Diaz, E., Rouillard, A. P., Davies, J. A., et al. 2017a, ApJ, 851, 32
Sanchez-Diaz, E., Rouillard, A. P., Davies, J. A., et al. 2017b, ApJL, 835, L7
Schatten, K. 1971, CosEl, 2, 232
Schwadron, N. A., & McComas, D. J. 2008, ApJL, 686, L33
Scott, R. B., Pontin, D. I., Yeates, A. R., Wyper, P. F., & Higginson, A. K. 2018, ApJ, 869, 60
Sheeley, J. N. R., & Wang, Y. M. 2007, ApJ, 655, 1142
Sheeley, J. N. R., Wang, Y.-M., Hawley, S. H., et al. 1997, ApJ, 484, 472
Sheeley, N. R., Lee, D. D. H., Casto, K. P., Wang, Y. M., & Rich, N. B. 2009, ApJ, 694, 1471
Sheeley, N. R., & Rouillard, A. P. 2010, ApJ, 715, 300
Sheeley, N. R., Walters, J. H., Wang, Y. M., & Howard, R. A. 1999, JGRA, 104, 24739
Shen, C., Chi, Y., Wang, Y., Xu, M., & Wang, S. 2017, JGRA, 122, 5931
Song, H. Q., Kong, X. L., Chen, Y., et al. 2012, SoPh, 276, 261
Suzuki, T. K., & Inutsuka, S.-i 2006, JGRA, 111, A06101
Telloni, D., Zank, G. P., Stangalini, M., et al. 2022, ApJL, 936, L25
Thernisien, A. 2011, ApJS, 194, 33
Thernisien, A., Vourlidas, A., & Howard, R. A. 2009, SoPh, 256, 111
Thernisien, A. F. R., Howard, R. A., & Vourlidas, A. 2006, ApJ, 652, 763
Viall, N. M., DeForest, C. E., & Kepko, L. 2021, FrASS, 8, 139
Viall, N. M., & Vourlidas, A. 2015, ApJ, 807, 176
Volpes, L., & Bothmer, V. 2015, SoPh, 290, 3005
Vourlidas, A., & Howard, R. A. 2006, ApJ, 642, 1216
Vourlidas, A., Howard, R. A., Plunkett, S. P., et al. 2016, SSRv, 204, 83
Wang, J.-J., Luo, B.-X., Liu, S.-Q., & Gong, J.-C. 2013, ChJG, 56, 2871
Wang, Y., Bai, X., Chen, C., et al. 2023, AdSpR, 71, 1146

Wang, Y., Xue, X., Shen, C., et al. 2006, ApJ, 646, 625
Wang, Y. M., & Sheeley, N. R., Jr. 1990, ApJ, 355, 726
Wang, Y. M., Sheeley, N. R., Jr., Walters, J. H., et al. 1998, ApJL, 498, L165
Wang, Y. M., Ye, P. Z., Wang, S., & Xue, X. H. 2003, GeoRL, 30, 1700
Wexler, D., Imamura, T., Efimov, A., et al. 2020, SoPh, 295, 111

Xie, H., Ofman, L., & Lawrence, G. 2004, JGRA, 109, A03109
Xue, X. H., Wang, C. B., & Dou, X. K. 2005, JGRA, 110, A08103
Ying, B., Bemporad, A., Giordano, S., et al. 2019, ApJ, 880, 41
Zhao, X. P. 2008, JGRA, 113, A02101
Zhao, X. P., Plunkett, S. P., & Liu, W. 2002, JGRA, 107, 1223